RSC Advances

PAPER

View Article Online
View Journal | View Issue

Cite this: *RSC Adv.*, 2025, **15**, 48083

Interferometric optical sensors based on porous silicon grafted with styrenic moieties for highly enhanced VOC detection

Van-The Vo,[a] Abhijit. N. Kadam,[b] Thuy-An Nguyen*[cd] and Sang-Wha Lee *[e]

The majority of volatile organic compounds (VOCs) are hazardous pollutants that pose significant risks to human health and the environment. Thus, the development of a smart sensing system for the early identification of VOCs would be in high demand, particularly those enabling rapid detection with high sensitivity and long-term stability. In this study, an interferometric optical sensor was rationally devised through the facile non-atmospheric thermolysis of polystyrene (PS) pre-loaded into a porous silicon (pSi) template prepared *via* electrochemical anodization. During the thermolysis, styrenic carbon fragments were covalently grafted onto the pore walls of pSi to form a PS-grafted pSi composite (pSi-PS). This composite was subsequently utilized as a scaffold for grafting poly(4-chlorostyrene) (PPCS) *via* a second thermolysis step, consequently yielding the double-grafted pSi composite (pSi-PS-PPCS). The obtained samples were subsequently employed as an interferometric optical sensor for the sensitive detection of various VOCs, including ethanol, isopropanol, isobutanol, *n*-hexane, methyl ethyl ketone (M. E. K.), and ethyl acetate. The sensitivity of the optical response to those VOCs exhibited the following order: *n*-hexane < ethanol < isopropanol < M. E. K. < isobutanol < ethyl acetate. Notably, the double-grafted pSi-PS-PPCS sensor exhibited significantly higher sensitivity than both pristine pSi and single-grafted pSi-PS. The highly enhanced sensitivity of pSi-PS-PPCS, particularly toward isobutanol and ethyl acetate vapors, was mainly attributed to strong intermolecular interactions (such as hydrophobic, hydrogen bonding effects and/or strong interplay of π–π interactions) between the VOC analytes and the chlorine-substituted phenyl moieties of the grafted PPCS.

Received 24th September 2025
Accepted 27th November 2025

DOI: 10.1039/d5ra07263h

rsc.li/rsc-advances

1. Introduction

Since the discovery of efficient visible-light emission from porous silicon (pSi), pSi-based materials (pSiMRs) have been widely utilized in chemical sensors for applications spanning from medical diagnoses to environmental monitoring, industrial effluents, homeland security, and automotive segmentation[1,2] pSiMRs are highly advantageous for use in optoelectronic sensors because of their high surface area (~500 m^2 cm^{-3}),[3] facile surface functionalization,[4] visible luminescence at room temperature, and biocompatibility.[5,6] Desirable environmental and chemical sensors require good sensitivity and selectivity, which depend strongly on the adsorption affinity toward specific analytes, whereas the reproducibility is mainly dictated by the structural and chemical stability of the sensing substrate, which is determined by the fabrication methods.[7–9]

Extensive research on pSiMRs has explored diverse sensing mechanisms, including optical reflectivity,[4,10] capacitance,[11,12] photoluminescence,[13,14] electrical resistance,[15,16] and electrochemical sensing.[17,18] pSi matrices with tunable grafting densities have shown promise as sensitive optical interferometric platforms for detecting analytes through Fabry-Perot fringe-shifts induced by analyte adsorption.[19–21] When the analyte is adsorbed on the pore walls, the refractive index of the porous matrix increases, resulting in a red shift in the optical spectrum. Thus, interferometric optical sensing is actively employed for the detection of trace-level VOCs that are frequently encountered in environmental pollution monitoring.[22–24] Ghaderi, *et al.*[25] fabricated porous silicon *via* an electrochemical etching process using a HF/ethanol electrolyte at different ratios. The study illustrated that the porosity contributes to reducing the steepness values because of heightened dislocations and structural disturbances. The transconductance parameter reverses with the strength of the electron–phonon interaction and porosity. When used as a sensor for CO_2 and O_2 at room temperature, notable changes

[a]*Long Son Petrochemicals Co., Ltd, Central Laboratory Department, Ho Chi Minh City, Vietnam*

[b]*Department of Chemistry, Wilson College (Autonomous), Mumbai 07, India*

[c]*Institute of Fundamental and Applied Sciences, Duy Tan University, Ho Chi Minh City 70000, Vietnam. E-mail: nguyenthuyan3@duytan.edu.vn*

[d]*Faculty of Environmental and Chemical Engineering, Duy Tan University, Da Nang City 50000, Vietnam*

[e]*Department of Chemical and Biological Engineering, Gachon University, South Korea. E-mail: lswha@gachon.ac.kr*

were apparent, wherein the electrical resistance decreased with increasing gas concentration. Shanu *et al.*[26] fabricated free-standing pSi (FS-pSi) *via* an etching process for chemical sensing *via* reflection/transmission (R/T) with a white-light source, demonstrating that FS-pSi microcavities can be used for detecting various volatile solvents based on the change in the peak position of the cavity mode, leading to changes in the refractive index. They found that the peak shift was directly correlated with the change in the refractive index. Mehta *et al.*[27] presented the novel application of a plasmonic microdisk resonator for the detection of methanol vapor. The sensor afforded a sensitivity of 308.94–569.52 nm per RIU, figure of merit (FoM) of 46.16–135.66 RUI^{-1}, and high *Q*-factor of *ca.* 370 at 5–20% porosity (pSi).

Korotcenkov and Rusuv[28] reviewed the potential of pSi as an inexpensive platform for advanced and sensitive gas and vapor sensors. However, realizing these objectives was difficult because of the insufficient stability of pSi and the low selectivity and poor reproducibility of the sensor signals. Therefore, the development of stable and reversible sensors capable of detecting various gases and vapors is necessary. Zhang *et al.*[29] constructed a photonic nose for the detection and discrimination of VOCs by infiltrating a specific type of ionic liquid (IL) into the pore channel of a patterned pSi chip. The ILs/pSi sensor array produced a unique, cross-reactive "fingerprint" in response to a specific type of VOC analyte. The sensor exhibited good stability and reproducibility over 11 cycles, with a long shelf-life (greater than one and a half years) owing to the high thermal stability of the IL. Ruminski *et al.*[4] systematically studied the effect of surface modification on the spectral shift of the resonance wavelength of a rugate filter upon exposure to VOCs. Thermal oxidation and acetylene carbonization led to acceptable stability and different responses to isopropyl alcohol (IPA) and heptane vapor, with a linear response range of 50–800 ppm. However, despite advancements in surface modification and tailored nanostructure technologies, pSi still suffers from limited physicochemical stability under humid and corrosive conditions.[30,31]

In this context, hydrosilylation reactions can improve the chemical stability of pSi, wherein unsaturated bonds are inserted into the Si–H groups. The resulting formation of robust Si–C bonds provides sustainable protection against nucleophilic attacks in aqueous or corrosive environments.[32,33] However, hydrosilylation grafting generally leads to undesirable short-term stability, owing to the partial derivatization (20–30%) of the surficial Si–H bonds.[32] Other methods of forming stable Si–C bonds include radical coupling in non-aqueous solvents, complex electrochemical alkylation, and thermal carbonization at high temperatures.[9,34–36] These strategies require sophisticated control of the reaction parameters under harsh conditions and do not readily provide a stable interface with tunable surface functionalization. Furthermore, pSi materials are readily oxidized and exhibit poor performance during continuous operation under ambient conditions for long periods.[13]

Porous silicon nanostructure (pSi) has unique properties such as tunable porosity, tailorable surface chemistry, optical reflectivity, and photoluminescence.[37–41] The porous layer of pSi can provide not only very high surface area for analyte adsorption (up to a few $m^2\ cm^{-3}$), but also porous template for polymer infiltration.[42–47] Analytes adsorbed on the internal surface of pSi can affect its refractive index, optical interference,[48–50] and photoluminescence, dielectric constant.[51–53] Meanwhile, pSiMRs play as a sensory optical material for gas detection, utilizing various conjugated emissive polymers with a high quantum yield.[54–56] In addition, pSiMRs with grafted styrenic polymers exhibited outstanding stability under harsh conditions and excellent recyclability over a long-period time.

In this work, thermolytic grafting was employed in fabricating a stable and strongly adsorbed interlayer on pSi. Electrochemically anodized pSi was infiltrated with 10 wt% polystyrene (PS) solution in toluene, followed by thermolytic degradation at 380 °C under inert atmosphere, yielding PS-grafted pSi (pSi-PS). This was subsequently used as a template for a second thermolysis with poly(4-chlorostyrene) (PPCS) at 360 °C, producing a PPCS-grafted pSi-PS composite (pSi-PS-PPCS). The outstanding stability of the double-polymer-grafted chips under HF corrosion illustrated that the grafted layer minimized adventitious oxidation of the pSi surface. The resulting materials exhibited interferometric optical responses to various VOCs, where the sensitivity increased in the following order: hexane < ethanol < isopropanol < methyl ethyl ketone (M. E. K) < isobutanol < ethyl acetate. Notably, double-grafted pSi-PS-PPCS exhibited enhanced sensitivity compared to single-grafted pSi-PS, mainly because of stronger interactions (such as hydrophobic, hydrogen bonding effects and/or strong interplay of π–π interactions) between the VOC analytes and the chlorine-substituted phenyl rings. These pSi-based composites demonstrate effective VOC detection and discrimination *via* optical interferometry.

2. Experimental

2.1. Materials

Highly boron-doped, p-type silicon wafers (resistivity 1–3 mΩ cm, orientation (100), 500–550 μm thickness) were obtained from Virginia Semiconductor, Inc. Hydrofluoric acid (HF) (48% aqueous, ACS grade), absolute ethanol (EtOH), polystyrene (analytical standard for GPC, M_w = 20 kDa), poly(4-chlorostyrene) (analytical standard for GPC, M_w = 75 kDa), isopropanol, *n*-hexane, isopropanol, isobutanol, M. E. K., and ethyl acetate were purchased from Sigma-Aldrich. All chemicals were used as received without further purification.

2.2. Preparation of porous silicon

Porous silicon (pSi) chips (porosity of 60–70%) were prepared by electrochemical etching of silicon wafers in an electrolyte consisting of a 3 : 1 (v/v) mixture of 48% aqueous HF : EtOH[57] Galvanostatic etching was carried out in a Teflon cell with a platinum counter electrode. A silicon wafer was used as the working electrode with an exposed area of 8.6 cm^2, and the back side was in contact with aluminum foil. The Si wafer was etched at a current density of 100 mA cm^{-2} for 3 min. The pSi chip was

then rinsed with ETOH several times and dried under a stream of nitrogen gas.

2.3. Fabrication of pSi composites

The thermolytic grafting of polystyrene (PS) was performed by the following procedures.[57] The freshly etched pSi chip was placed on a hot plate at 70 °C, after which 20 μL of PS solution (10 wt% in toluene) was dropped onto the preheated pSi and maintained at 70 °C for 5 min. The temperature of the hot plate was then increased to 110 °C and kept for 10 min to facilitate the infiltration of PS into the pSi. The PS-infiltrated pSi sample was placed in a tube furnace under N_2 flow (2.0 L min^{-1}) and kept for 30 min. The furnace temperature was ramped to 380 °C at a rate of 10 °C min^{-1}, maintained at this temperature for 1 h, and then cooled to room temperature under N_2 flow. The resulting PS-grafted pSi (pSi-PS) was soaked in toluene for 2 h to remove the unreacted polymer residues. The thermolytic grafting of PPCS was performed under otherwise identical conditions. That is, 20 μL of PPCS (5.0 wt% in toluene) was dropped onto the pSi-PS template and subjected to thermolysis at 360 °C for 1 h to obtain the PPCS-grafted pSi-PS (pSi-PS-PPCS). The final pSi samples were then soaked in toluene for 30 min to remove any residual non-grafted polymer fragments, rinsed with excess ETOH, and dried under nitrogen flow prior to further characterization. The characterization of the pSi samples is described in the SI.

2.4. VOC sensing tests

The VOC sensing system was operated using a binary bump system with a nitrogen transporter.[4] The system contained two pumps: one pump for passing nitrogen through a volatile organic solvent to generate vapor in a gas bubbler, and the other pump containing only pure nitrogen gas (Scheme S1). The total flow rate of the two pumps was maintained at 500 sccm. The two flows were collected in Erlenmeyer flasks to obtain a homogeneous mixture. This mixture was then passed through a pSi chip mounted on a gas flow cell. Reflectance spectra were recorded from the chip surface every two minutes. The organic solvent was sparged with pure nitrogen gas at flow rates ranging from 0.5 to 8.5 sccm. Each measurement was initiated after purging with nitrogen gas for 30 min to ensure that no VOCs remained in the system. VOC detection was performed in triplicate at each concentration. The measured reflectance was transformed into the optical thickness using the fast Fourier transform (FFT) method. The average value of the peak shift was then calculated as the difference in the optical thickness from the reflectance spectra before and after the VOC flow.

3. Results and discussion

3.1. Synthesis and characterization of as-prepared pSi samples

Scheme 1 shows the fabrication steps, from electrochemical etching of the crystalline silicon wafers to formation of the porous silicon composites, and the final application of the optical reflectance-based interferometric analysis to VOC analytes. More specifically, the electrochemically anodized pSi chip was infiltrated with polystyrene (PS), and the PS-loaded pSi was placed into a tube furnace under N_2 flow for 1 h. Thermolysis of the infiltrated PS generated styrenic fragments that were readily grafted onto the surface of pSi *via* hydrosilyation-type and/or radical coupling with the hydrogen-terminated silicon surface, forming the PS-grafted pSi (pSi-PS) composite.[47,57,58] The pSi-PS composite was then used as the second template for another PPCS grafting under non-atmospheric thermolysis at 360 °C. The resulting product is referred to as the PPCS-grafted pSi-PS (pSi-PS-PPCS) composite. Finally, the as-obtained pSi samples (pSi, pSi-PS, and pSi-PS-PPCS) were used for the detection of various VOCs using an interferometric reflectance system (Scheme S1).

Fig. 1 shows the FTIR spectra of the prepared samples. As illustrated in Scheme 1, freshly-etched (pristine) pSi (62% porosity) was first grafted with PS *via* thermolysis at 380 °C, denoted as the pSi-PS composite (42% porosity). Thereafter, pSi-PS was grafted with PPCS *via* a second thermolysis step at 360 °C to give the pSi-PS-PPCS composite (37% porosity). The FTIR

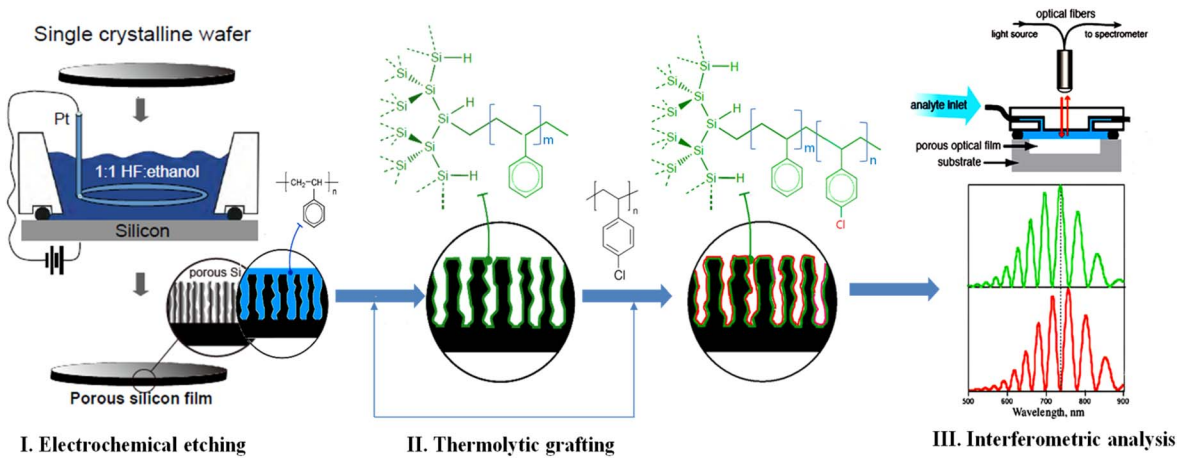

Scheme 1 Overall fabrication steps for electrochemical etching of crystalline silicon wafer, thermolysis of porous silicon composites, and a sensing device for optical reflectance-based interferometric measurements.

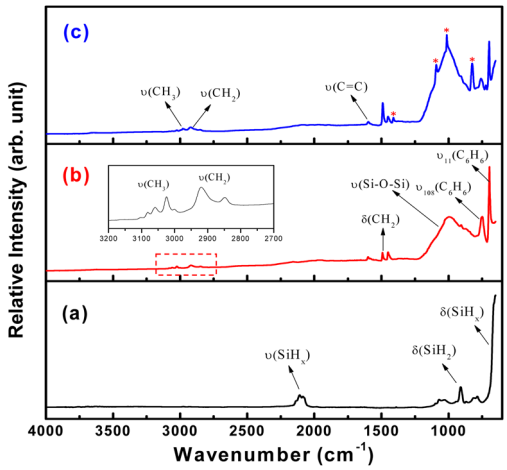

Fig. 1 FTIR spectra of (a) pSi, (b) pSi-PS, and (c) pSi-PS-PPCS samples. All samples were soaked in toluene for 2 h to remove unreacted polymer, followed by treatment with 0.8% HF (15 min) to remove silica oxides.

spectrum of pristine pSi (Fig. 1(a)) shows several characteristic bands of the silicon hydride groups. The characteristic vibrational modes of the Si–H species were assigned as follows: ν(Si–H_x) stretching vibrations at 2108 cm^{-1},[59] δ(Si–H_2) scissoring mode at 913 cm^{-1},[60] and ν(Si–H_x) deformation mode at 665 cm^{-1}.[33,57,61] The FTIR spectrum of the pSi-PS composite (Fig. 1(b)) demonstrated several characteristic FTIR bands of the styrenic fragments originating from PS, revealing a loss of Si–H_x species (2108 cm^{-1}), a substantial appearance of Si–O stretching vibrations at 1040 cm^{-1}, and a distinct $\nu_{11}(C_6H_6)$ peak at 690 cm^{-1}. Notably, the vibrational bands of the in-plane phenyl groups of the C–C skeleton appeared at 1590, 1490, and 1447 cm^{-1}. The magnified FTIR bands in the range of 2800–3200 cm^{-1} correspond to the distinct asymmetric and symmetric C–H stretching vibrations of aliphatic –CH_2– at 2920 cm^{-1} and 2850 cm^{-1}, respectively. In addition, the stretching vibrations of aliphatic –CH_3 at 3025 cm^{-1} are apparent in the inset of Fig. 1(b). The FTIR spectra of the pSi-PS-PPCS composite displayed signals of the styrenic fragments originating from the firstly grafted PS as well as additional peaks of the secondly grafted PPCS at 1409, 1100, 1010, and 818 cm^{-1}. Notably, the intensity of the peak at 1489 cm^{-1} increased distinctly after the second PPCS grafting, indicating that the PPCS fragments were conjoined with the PS fragments that were previously grafted on the pSi surface.[62,63] Despite the inert atmosphere used in the thermolysis process, intrinsic and/or leaked oxygen induced the appearance of a Si–O stretching band in the spectra of the pSi samples.

The stability of the grafted pSi composites under HF corrosion was confirmed by HF treatment under various conditions. Fig. S1 presents a comparison of the FTIR spectra of the pSi-PS and pSi-PS-PPCS composites after removing the unreacted polymer residues by soaking in toluene, followed by strong HF treatment to remove the Si–O layer. Fig. S1(A) shows the FTIR spectrum of the pSi-PS composite, illustrating several characteristic bands attributed to the styrenic carbons of PS. The most distinct peaks at 698 and 757 cm^{-1} are attributed to the C–C and C–H out-of-plane bending modes, respectively. In addition, three characteristic C–C skeletal in-plane phenyl vibrational bands appeared at 1600, 1492, and 1452 cm^{-1}, and the peaks in the magnified FTIR window are assigned to the asymmetric and symmetric C–H stretching vibrations of aliphatic –CH_3 and –CH_2– at 2923 and 2851 cm^{-1}, respectively. A distinct Si–O stretching band was also observed at 1030 cm^{-1}, owing to the adventitious formation of silicon oxide during thermolysis at the elevated temperature of 360 °C.

Fig. S1(B) presents the FTIR spectra of the pSi-PS-PPCS composite after soaking in toluene for 2 h, which showed peaks of styrenic carbons originating from PS grafting, as well as new peaks at 1411.5, 1093.0, 1011.9, and 820 cm^{-1} that were attributed to PPCS grafting. Notably, the peak intensity at 1492 cm^{-1} increased to a greater extent than that of the pSi-PS composite. After treating pSi-PS-PPCS with 0.8% HF(aq.) in 10% ethanol (15 min) (Fig. S1C), these peaks became more apparent owing to the removal of the silicon oxide layer. To confirm the covalent Si–C grafting, pSi-PS-PPCS was treated with 40% HF solution for progressively longer times (from 10 min to 4 h). As shown in Fig. S1(D), the stronger HF treatment selectively dissolved the silicon oxides while leaving the Si–C grafts intact. Consequently, the Si–O band almost disappeared, whereas the vibrational bands of the styrenic carbons in the Si–C bonds remained more intense without any apparent decrease. The FTIR spectra of pSi-PS-PPCS after the strong HF treatment illustrated that the styrenic carbons were covalently bound to the pSi surface *via* Si–C bonds, with excellent chemical stability against strong HF attack.

The pore size decreased upon grafting the styrenic fragments, as shown in Fig. 2(a–c) and S2. However, the difference in the pore size of the pSi-PS and pSi-PS-PPCS composites was not pronounced, possibly owing to the similar porosities of these samples, as determined by the spectroscopic liquid infiltration method (SLIM).[33] From the SLIM test, the porosities of pSi, pSi-PS, and pSi-PS-PPCS were estimated as 61%, 42%, and 37%, respectively. The surface morphologies of the pSi samples were well-maintained even after thermolytic grafting. Meanwhile, the cross-sectioned porous layer is *ca.* 9.3 μm and maintained well during thermalytic grafting and the subsequent HF treatment, as shown in Fig. S3. Energy-dispersive X-ray spectroscopy (EDS) was used to evaluate the uniformity of the distribution of the grafted components. EDS mapping showed the presence of Si, C, and Cl, demonstrating successful grafting of the styrenic fragments onto the pSi surface. The distribution of carbon in double-grafted pSi (pSi-PS-PPCS) was more uniform and dense than that in single-grafted pSi (pSi-PS). EDS mapping also revealed the presence of chlorine in pSi-PS-PPCS, confirming the successful grafting of PPCS onto the pSi-PS composite. The samples were analyzed by SEM (SU8600; Smart Materials Research Center for IoT supported by the Korea Basic Science Institute, NFEC-2023-02-285654).

Fig. 3 shows the reflectance spectra of the pSi samples, where the maximum peak for pristine pSi was observed at 680 nm, whereas that of the pSi-PS and pSi-PS-PPCS composites appeared at 670 and 660 nm, respectively. The maximal peak of

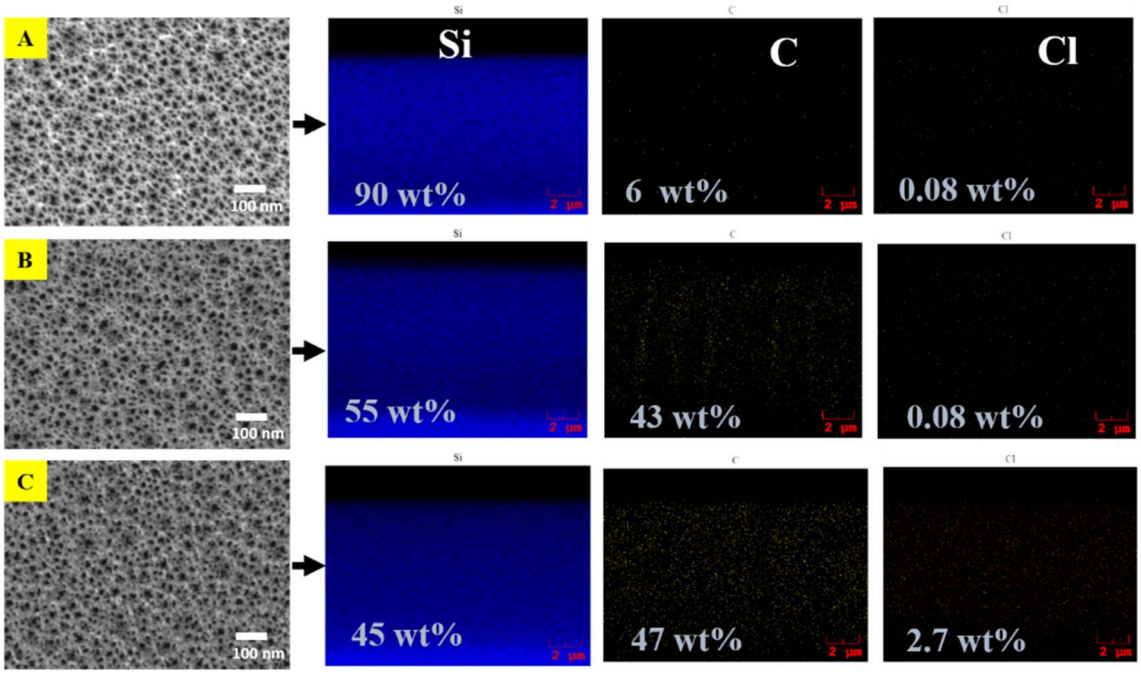

Fig. 2 Scanning electron microscope (SEM) images; columns show corresponding EDX maps of Si, C, and Cl components: (A) pristine pSi (porosity = 61%), (B) pSi-PS composite (porosity = 42%), (C) pSi-PS-PPCS composite (porosity = 37%).

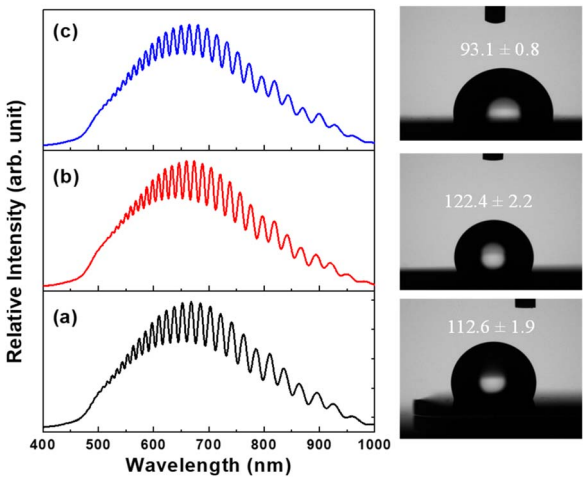

Fig. 3 Reflectance spectra of as-prepared samples. The water contact angles (CAs) of the (a) pSi, (b) pSi-PS, and (c) pSi-PS-PPCS chips are 112.6 ± 1.9, 122.4 ± 2.2, and 93 ± 0.8, respectively.

the pSi composites was blue-shifted by 10–20 nm, plausibly owing to the decrease in the porosity caused by the grafted styrenic fragments. Fig. S4 shows the Raman spectra of the pSi samples within the range of 350–1200 cm^{-1}. The peak position and linewidth were similar for all the pSi samples, *i.e.*, the Si peak was located at 516–517 cm^{-1}. For all the pSi samples, the peak exhibited asymmetric broadening compared with that of crystalline Si. The control sample (oxidized pSi) was prepared under identical conditions using freshly etched pSi without polymer infiltration. No distinct peak or shoulder attributable to the amorphous region appeared around 480 cm^{-1}. Thus, the asymmetric Lorentzian shape of the Raman spectra can be attributed to the oxide layer formed on the Si surface.[64,65]

The right panel in Fig. 3 shows the water contact angle (WCA) of the pristine pSi, pSi-PS, and pSi-PS-PPCS composites. The WCA of pristine pSi was measured immediately after etching the Si wafer to minimize the effect of oxidation on the WCA. The WCAs of the pSi samples decreased in the following order: pSi-PS (122.4°) > pSi (112.6°) > pSi-PS-PPCS (93.6°). The WCA of pSi-PS was higher than that of pSi and pSi-PS-PPCS. The increase in the WCA of pSi-PS was attributed to the grafting of non-polar PS, and the decrease in the WCA of pSi-PS-PPCS was attributed to the grafting of polar PPCS. Therefore, PPCS-grafted pSi-PS (pSi-PS-PPCS) exhibits a lower WCA than PS-grafted pSi (pSi-PS).

3.2. Interferometric sensing of various VOCs using grafted pSi samples

Interferometric sensing is based on the adsorption of analytes onto porous walls. The adsorption of an analyte on porous channels occurs *via* two main mechanisms: (i) microcapillary condensation and (ii) surface sorption (physisorption) through van der Waals forces.[66,67] Microcapillary condensation, in which vapors spontaneously condense in microporous and mesoporous matrices, can be described by the Kelvin equation: microcapillary condensation is effective at high analyte vapor pressures in the high-ppm range, whereas physisorption is the major mechanism responsible for the optical response at low vapor pressures in the mid/low-ppm range. Thus, it is reasonable to expect that VOC analytes can be adsorbed onto high-surface-area pSi in the mid-to-low-ppm range, leading to an observable spectral shift of the Fabri-Perot fringes.

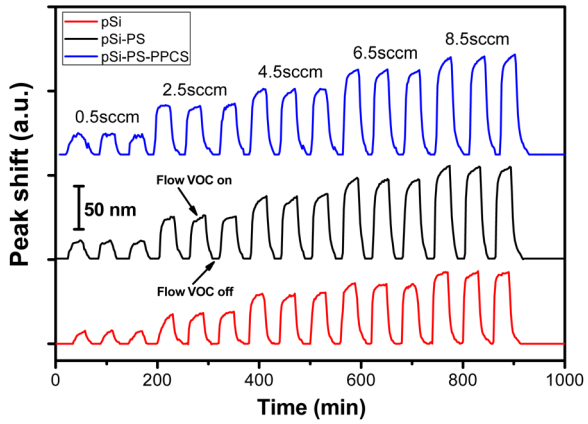

Fig. 4 Peak shift of the samples in response to the flow rate of M. E. K. vapor (VOC flow and N_2 purging periods).

The as-prepared pSi samples (pSi, pSi-PS, and pSi-PS-PPCS) were tested as interferometric sensors for detecting trace VOC analytes. Fig. 4 shows the peak shift of the Fabri-Perot fringes of the pSi, pSi-PS, and pSi-PS-PPCS samples, corresponding to the alternating flow of the M. E. K. analyte and purging N_2 gas.

The average peak-shift increased in the order: pSi < pSi-PS < pSi-PS-PPCS, indicating that pSi-PS-PPCS exhibited higher sensitivity to M. E. K. vapor than the other pSi samples. At a low flow rate (0.5 sccm), pSi, pSi-PS, and pSi-PS-PPCS exhibited peak shifts of 4.4, 6.6, and 23.2 nm, respectively. The significant difference in the optical thickness indicates a strong dependence of the interferometric sensitivity of the VOCs on the characteristic surface modifications of the pSi samples. Thermolysis of the infiltrated polymers produced styrenic fragments that were subsequently tethered to the pore walls, with uniform pore filling. In contrast, pristine pSi has only Si–H and Si–O bonds, which have low affinity for organic VOCs. Double-grafted pSi has styrenic carbons rich in phenyl rings that participate in strong intermolecular interactions with organic M. E. K. vapor. Moreover, double-grafted pSi exhibited higher sensitivity than single-grafted pSi, possibly because of the higher grafting density of styrenic carbons rich in phenyl rings.

In practice, the pSi chip exhibits a critical limitation in achieving stable interferometric sensing of VOC analytes. Thus, the pSi was grafted with non-polar PS and the resulting PS-grafted pSi (pSi-PS) shows stable sensing performance for various VOC analytes with high sensitivity. In addition, the WCA of pSi-PS was increased due to the contribution hydrophobic nature of grafted PS moieties and the presence of air pockets within the porous nanostructure. After that, the pSi-PS was doubly grafted with polar PPCS, which further increased the overall grafting density of the combined PS and PPCS moieties. Notably, the water WCA on the double-grafted pSi (pSi-PS-PPCS) was lower than that of single-grafted pSi (pSi-PS), probably due to the increased oxidation of Si template by repeated thermolysis at elevated temperature. In addition, the lower WCA of the pSi-PS-PPCS compared to pSi-PS is mainly due to the increased polar fractions by the grafted PPCS moieties, consequently leading to the enhanced wettability.

Furthermore, double-grafted pSi has styrenic carbons rich in phenyl rings that can participate in strong intermolecular interactions with VOCs vapor, whereas pristine pSi has only Si–H and Si–O bonds, which have low affinity for organic VOCs. The distinct peak shifts clearly indicated that modified Si surface induced more adsorption of aromatic vapors, likely due to the enhanced interactions between the analytes and styrenic carbons rich of phenyl rings. According to Wheeler–Houk model, π–π stacking interactions between substituted phenyl rings are enhanced irrespective of the types of substituents (or heteroatoms), and substituted phenyl rings can induce the stronger interaction than phenyl rings without substitutions.[68,69] Thus, double-grafted pSi with para-substituted phenyl rings can produce the larger peak shifts by inducing larger adsorption of aromatic VOCs than that of single-grafted pSi with substituent-free phenyl rings. To be conclusive, the sensitivity for VOCs is mainly influenced by the strong interplay of π–π interactions between grafted phenyl rings and VOCs analytes;

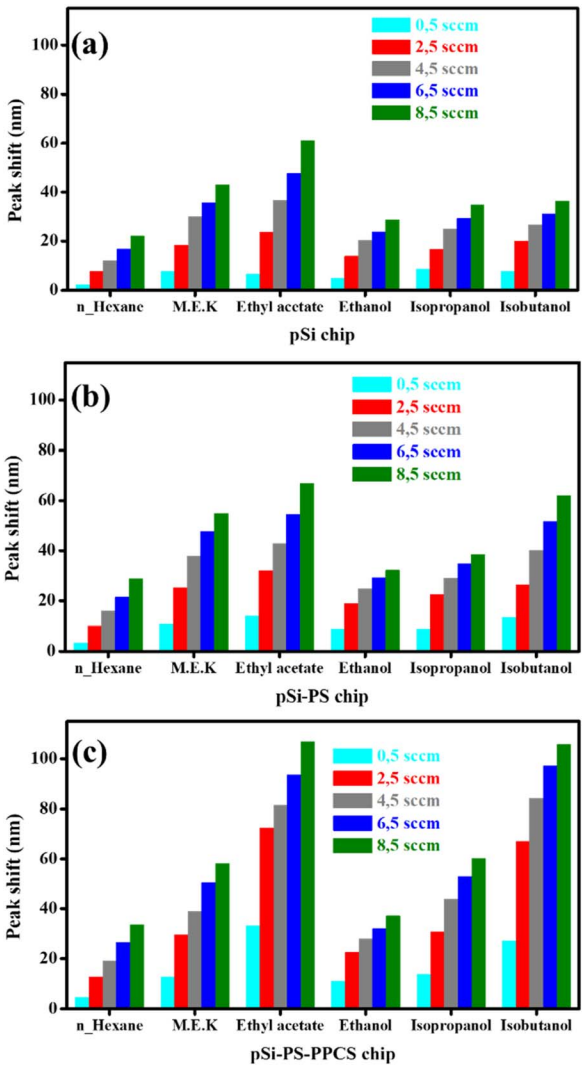

Fig. 5 Comparison of optical responses of the chip sensor against different types of VOCs: (a) pSi chip, (b) pSi-PS chip and (c) pSi-PS-PPCS chip.

the grafting moieties of hydrophobic and hydrophilic phenyl rings can strongly influence on the sensing performance of pSi-based composites.

Fig. 5 presents a comparison of the peak shifts of all the pSi samples for the interferometric sensing of various VOCs (hexane, ethyl acetate, ethanol, M. E. K., isopropanol, and isobutanol) with increasing flow rate of the VOCs (Fig. S5). pSi-PS-PPCS (Fig. 5(c)) demonstrated higher sensitivity and quicker responses for all the VOCs, compared with pristine pSi and pSi-PS (Fig. 5(a and b)).

For all pSi samples, the interferometric sensitivity (*i.e.*, peak-shift values) increased in the order: hexane < ethanol < isopropanol < M. E. K. < isobutanol < ethyl acetate. The sensitivity for the VOCs also increased in the following order: pSi < pSi-PS < pSi-PS-PPCS. As summarized in Fig. 5(c), pSi-PS-PPCS exhibited distinct changes in the optical thickness (a large peak shift) when exposed to isobutanol and ethyl acetate vapors, possibly owing to the strong interactions between these two analytes and the phenyl rings with greater polarity. For example, long-carbon-chain alcohols can undergo greater hydrophobic interactions with styrenic carbon rich in phenyl rings, as compared to low-carbon alcohols (such as ethanol and isopropanol). On the other hand, oxygen-containing VOCs can undergo stronger polar interactions with chlorine-substituted phenyl carbons, consequently leading to higher interferometric sensitivity to ethyl acetate vapor. For instance, the chlorine atom makes the phenyl ring more electron-deficient through its electron-withdrawing inductive effect. The resonance structure of ethyl acetate can facilitate hydrogen bonding interactions with the chlorine-substituted phenyl rings,[70–72] as illustrated in Fig. S6. Thus, the intermolecular interaction energies were generally in the range of 2–4 kcal mol^{-1}, which is roughly half of the energetic stabilization of conventional H-bonds.[73,74]

Fig. 6 shows the three-dimensional (3-D) projection plots for the optical responses of pSi-PS-PPCS exposed to various VOCs at 0.5 sccm. The observed peak shifts for ethyl acetate, isobutanol, methyl ethyl ketone, isopropanol, ethanol, and hexane were 33.17, 27.59, 15.35, 13.73, 11.23, and 4.74 nm, respectively, which were distinct even at trace-level concentration. Typically, VOCs with higher volatility tend to condense in nanostructured pores, resulting in more pronounced optical responses. Interestingly, although the vapor pressure of hexane is higher than that of ethyl acetate, the latter induced a peak shift that was nearly eight times larger. This indicates a strong molecular interaction between ethyl acetate and the styrenic moieties grafted onto the pSi surface. Moreover, despite the similar polarity indices of isobutanol and isopropanol (~3.9), the peak shifts of isobutanol (27.59 nm) and isopropanol (13.73 nm) differed significantly. This disparity likely arises from enhanced hydrophobic interactions between the longer alkyl chain of isobutanol and the hydrophobic polymer matrix. Ethanol, having a higher polarity index (~5.2), yielded a relatively smaller peak shift (11.23 nm), possibly because of its shorter carbon chain length, which limits hydrophobic interactions.

In addition, the ethanol-sensing performance of the pSi-PS-PPCS chip was compared with other representative sensor materials listed in Table S1. For example, Ryusei Sogame *et al.*[75] synthesized a freestanding membrane of Parylene C and polymethylmethacrylate (PMMA) on a Si substrate for EtOH detection. When the concentration of EtOH gas was 2.5 vol%, the reflection spectrum shifted by 38.8 nm to shorter wavelengths. Or Mingqi Gu *et al.*[76] presented an EtOH gas sensor based on a fiber ring laser system by coperation of Sagnac loop embedded with a nematic liquid crystal (NLC) film. This sensor system exhibited a detection limit of 247.42 ppm for EtOH gas, *etc.* however, the fabricated processes of previously reported methods were often complicated with relatively high detection limits and long operation times. These comparative studies clearly highlight the superior performance of our sensor chip.

Among the tested analytes, ethyl acetate exhibited the strongest optical response, which can be attributed to the following factors: (i) its resonance-stabilized acetate group that promotes hydrogen bonding with the chlorine-substituted phenyl moieties in the polymer matrix, (ii) the distinctive porous architecture of the double-grafted polymer chips, and (iii) the presence of multiple surface elemental states that provide abundant active sites for analyte adsorption.[77]

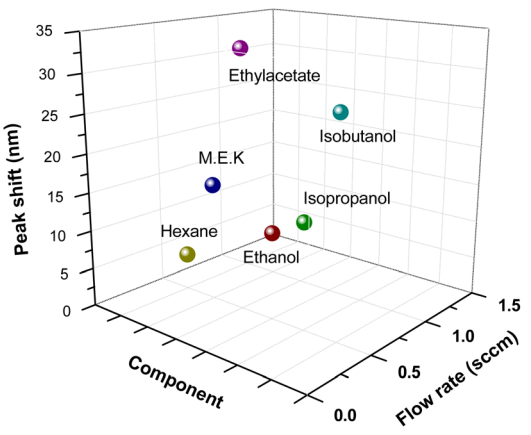

Fig. 6 Three-dimensional component analysis plots obtained from the optical response of pSi-PS-PPCS to various VOCs at 0.5 sccm. The plot demonstrates that each VOC can be well-distinguished.

4. Conclusions

Phenyl-ring-carbon-grafted pSi chips were successfully prepared and applied in the sensitive interferometric detection of six different VOCs. Briefly, the pSi template was infiltrated with polystyrene, and the PS-infiltrated pSi was transformed into PS-grafted pSi (pSi-PS) *via* non-atmospheric thermolysis at 380 °C for 1 h. PPCS was then doubly grafted onto the pSi-PS composite under otherwise identical conditions to obtain the so-called pSi-PS-PPCS. As a promising interferometric sensor for trace VOCs, the double-grafted pSi (pSi-PS-PPCS) exhibited larger peak shifts for all VOCs compared to pristine pSi and single-grafted pSi (pSi-PS). Thermolytic grafting induced the formation of covalent Si–C bonds on the pSi surface with a more stable interface. Double grafting was more beneficial for enabling the classification (or identification) of various VOCs as well as providing more specificity for the sensitive detection of VOCs.

Author contributions

Van-The Vo (V.-T. Vo): methodology, investigation, formal analysis writing – original draft; Abhijit. N. Kadam (A. N. Kadam): methodology, investigation, formal analysis; Thuy-An Nguyen (T.-A. Nguyen): conceptualization, supervision, writing – review, & editing; Sang-Wha Lee (S.-W. Lee): conceptualization, supervision, writing – review, & editing, resources, funding acquisition.

Conflicts of interest

There are no conflicts to declare.

Data availability

The data supporting this article have been included as part of the supplementary information (SI). No additional datasets or code were generated or analyzed during this study. Supplementary information: instrumental analysis, RIFTS method, schematic set up of VOCs detection system, FTIR spectra of the pSi samples at selected stages of preparation, SEM image of pSi composites at different magnifications, cross-sectional SEM images (pSi, pSi-PS-PPCS), Raman spectra of pSi composites, peak shift spectra of pSi composites corresponding to the different VOCs, plausible hydrogen-bonding interaction mechanism between chlorine-substituted phenyl ring and resonant ethyl acetate, comparison sensor performance for ethanol between pSi-PS-PPCS chip with other sensor materials. See DOI: https://doi.org/10.1039/d5ra07263h.

Acknowledgements

This research was supported by Basic Science Research Program through the National Research Foundation of Korea (NRF) funded by the Ministry of Education(No. RS-2021-NR060117). This research was also supported by the Gachon University research fund of 2025 (GCU-202503270001).

References

1 C. G. Siontorou, *Handbook of Cell Biosensors*, 2019, pp. 1–16.
2 T. Kumeria, J. Wang, N. Chan, T. J. Harris and M. J. Sailor, *ACS Sens.*, 2018, **3**, 143–150.
3 R. Herino, G. Bomchil, K. Barla, C. Bertrand and J. L. Ginoux, *J. Electrochem. Soc.*, 1987, **134**, 1994–2000.
4 A. M. Ruminski, B. H. King, J. Salonen, J. L. Snyder and M. J. Sailor, *Adv. Funct. Mater.*, 2010, **20**, 2874–2883.
5 A. G. Cullis, L. T. Canham and P. D. J. Calcott, *J. Appl. Phys.*, 1997, **82**, 909–965.
6 P. Fauchet, L. Tsybeskov, C. Peng, S. Duttagupta, J. Von Behren, Y. Kostoulas, J. Vandyshev and K. Hirschman, *IEEE J. Sel. Top. Quantum Electron.*, 1995, **1**, 1126–1139.
7 D. Kim, J. Joo, Y. Pan, A. Boarino, Y. W. Jun, K. H. Ahn, B. Arkles and M. J. Sailor, *Angew Chem. Int. Ed. Engl.*, 2016, **55**, 6423–6427.
8 D. Kim, J. M. Zuidema, J. Kang, Y. Pan, L. Wu, D. Warther, B. Arkles and M. J. Sailor, *J. Am. Chem. Soc.*, 2016, **138**, 15106–15109.
9 B. Sciacca, S. D. Alvarez, F. Geobaldo and M. J. Sailor, *Dalton Trans.*, 2010, **39**, 10847–10853.
10 A. Mehaney, M. M. Abadla and H. A. Elsayed, *J. Mol. Liq.*, 2021, **322**, 114978.
11 M. Archer, M. Christophersen and P. M. Fauchet, *Sens. Actuators, B*, 2005, **106**, 347–357.
12 F. A. Harraz, A. A. Ismail, H. Bouzid, S. A. Al-Sayari, A. Al-Hajry and M. S. Al-Assiri, *Appl. Surf. Sci.*, 2014, **307**, 704–711.
13 M. J. Sailor and E. C. Wu, *Adv. Funct. Mater.*, 2009, **19**, 3195–3208.
14 Y. Jung, S. Kang, J. An, J. Jung and D. Kim, *Dyes Pigm.*, 2020, **182**, 108700.
15 L. Seals, J. L. Gole, L. A. Tse and P. J. Hesketh, *J. Appl. Phys.*, 2002, **91**, 2519–2523.
16 D. Yan, S. Xia, S. Li, S. Wang, M. Tan and S. Liu, *Mater. Res. Bull.*, 2021, **134**, 111109.
17 M. Archer and P. M. Fauchet, *Phys. Status Solidi A*, 2003, **198**, 503–507.
18 A. A. Ensafi, F. Rezaloo and B. Rezaei, *Sens. Actuators, B*, 2016, **231**, 239–244.
19 C. L. Curtis, *J. Electrochem. Soc.*, 1993, **140**, 3492.
20 V. S. Lin, K. Motesharei, K. P. Dancil, M. J. Sailor and M. R. Ghadiri, *Science*, 1997, **278**, 840–843.
21 K.-P. S. Dancil, D. P. Greiner and M. J. Sailor, *J. Am. Chem. Soc.*, 1999, **121**, 7925–7930.
22 H. C. Menezes, L. C. A. Amorim and Z. L. Cardeal, *Crit. Rev. Environ. Sci. Technol.*, 2013, **43**, 1–39.
23 H. Zaitan, A. Korrir, T. Chafik and D. Bianchi, *J. Hazard. Mater.*, 2013, **262**, 365–376.
24 C. L. Wong, U. S. Dinish, M. S. Schmidt and M. Olivo, *Anal. Chim. Acta*, 2014, **844**, 54–60.
25 A. Ghaderi, J. Sabbaghzadeh, L. Dejam, G. Behzadi Pour, E. Moghimi, R. S. Matos, H. D. da Fonseca Filho, S. Talu, A. Salehi Shayegan, L. F. Aval, M. Astani Doudaran, A. Sari and S. Solaymani, *Sci. Rep.*, 2024, **14**, 3677.
26 M. Shanu, J. N. Acharyya, A. Kuriakose, D. Banerjee, V. R. Soma and G. Vijaya Prakash, *ACS Appl. Mater. Interfaces*, 2024, **16**, 16996–17006.
27 S. Mehta, N. N. B. V and M. Singh, *IEEE Sens. J.*, 2024, **24**, 12304–12311.
28 G. Korotcenkov and E. Rusu, *Phys. Status Solidi A*, 2019, **216**, 1900348.
29 H. Zhang, L. Lin, D. Liu, Q. Chen and J. Wu, *Anal. Chim. Acta*, 2017, **953**, 71–78.
30 M. Hecini, A. Khelifa, B. Bouzid, N. Drouiche, S. Aoudj and H. Hamitouche, *J. Phys. Chem. Solids*, 2013, **74**, 1227–1234.
31 T. K. Nguyen, S. Aberoumand and D. V. Dao, *Small*, 2021, **17**, e2101775.
32 J. M. Buriak, *Chem. Rev.*, 2002, **102**, 1271–1308.
33 M. J. Sailor, *Weinheim, Germany*, Wiley-VCH, 2012.
34 A. Bansal and N. S. Lewis, *J. Phys. Chem. B*, 1998, **102**, 4058–4060.

35 P. Allongue, C. H. de Villeneuve, J. Pinson, F. Ozanam, J. N. Chazalviel and X. Wallart, *Electrochim. Acta*, 1998, **43**, 2791–2798.
36 I. N. Lees, H. Lin, C. A. Canaria, C. Gurtner, M. J. Sailor and G. M. Miskelly, *Langmuir*, 2003, **19**, 9812–9817.
37 Y. Y. Li, F. Cunin, J. R. Link, T. Gao, R. E. Betts, S. H. Reiver, V. Chin, S. N. Bhatia and M. J. Sailor, *Science*, 2003, **299**, 2045–2047.
38 J. Harper and M. J. Sailor, *Anal. Chem.*, 1996, **68**, 3713–3717.
39 K. Urmann, S. Arshavsky-Graham, J. G. Walter, T. Scheper and E. Segal, *Analyst*, 2016, **141**, 5432–5440.
40 A. Daneshkhah, S. Shrestha, M. Agarwal and K. Varahramyan, *Sens. Actuators, B*, 2015, **221**, 635–643.
41 R. Thriumani, A. Zakaria, Y. Z. H. Hashim, A. I. Jeffree, K. M. Helmy, L. M. Kamarudin, M. I. Omar, A. Y. M. Shakaff, A. H. Adom and K. C. Persaud, *BMC Cancer*, 2018, **18**, 362.
42 K. L. Jarvis, T. J. Barnes and C. A. Prestidge, *Adv. Colloid Interface Sci.*, 2012, **175**, 25–38.
43 S. Dhanekar and S. Jain, *Biosens. Bioelectron.*, 2013, **41**, 54–64.
44 F. Buda, J. Kohanoff and M. Parrinello, *Phys. Rev. Lett.*, 1992, **69**, 1272–1275.
45 S. Jang, J. Kim, Y. Koh, J. Park, H. G. Woo, S. Kim and H. Sohn, *J. Nanosci. Nanotechnol.*, 2008, **8**, 5166–5171.
46 J. Salonen and E. Makila, *Adv. Mater.*, 2018, **30**, e1703819.
47 M. Xuan Tran, J.-Y. Woo, T.-A. Nguyen, S.-W. Lee and J. Kee Lee, *Chem. Eng. J.*, 2020, **395**, 125169.
48 R. F. Balderas-Valadez, M. Weiler, V. Agarwal and C. Pacholski, *Nanoscale Res. Lett.*, 2014, **9**, 425.
49 R. F. Balderas-Valadez, R. Schurmann and C. Pacholski, *Front. Chem.*, 2019, **7**, 593.
50 N. Abu-Thabit and E. Ratemi, *Front. Chem.*, 2020, **8**, 454.
51 T. S. Amran, M. R. Hashim, N. K. Al-Obaidi, H. Yazid and R. Adnan, *Nanoscale Res. Lett.*, 2013, **8**, 35.
52 G. Korotcenkov and E. Rusu, *Phys. Status Solidi A*, 2019, **216**, 1900348.
53 R. Wu, Q. Jin, C. Storey, J. Collins, G. Gomard, U. Lemmer, L. Canham, R. Kling and A. Kaplan, *Nanoscale Horiz.*, 2021, **6**, 781–790.
54 D. Wu, Y. Yu, J. Zhang, L. Guo and Y. Kong, *ACS Appl. Mater. Interfaces*, 2018, **10**, 23362–23368.
55 Y. Park, J. Yoo, M. H. Kang, W. Kwon and J. Joo, *J. Mater. Chem. B*, 2019, **7**, 6271–6292.
56 X. Gong, S. Zheng, X. Zhao and A. Vomiero, *Nano Energy*, 2022, **101**, 107617.
57 J. Wang, J. Joo, R. M. Kennard, S.-W. Lee and M. J. Sailor, *Chem. Mater.*, 2015, **28**, 79–89.
58 M. X. Tran, T.-A. Nguyen, J. K. Lee and S.-W. Lee, *J. Power Sources*, 2023, **554**, 232326.
59 Y. Ogata, H. Niki, T. Sakka and M. Iwasaki, *J. Electrochem. Soc.*, 1995, **142**, 195–201.
60 Y. Ogata, H. Niki, T. Sakka and M. Iwasaki, *J. Electrochem. Soc.*, 1995, **142**, 1595.
61 P. Gupta, A. Dillon, A. Bracker and S. George, *Surf. Sci.*, 1991, **245**, 360–372.
62 Y.-Y. Lua, W. J. J. Fillmore, L. Yang, M. V. Lee, P. B. Savage, M. C. Asplund and M. R. Linford, *Langmuir*, 2005, **21**, 2093–2097.
63 A. Sieval, A. Demirel, J. Nissink, M. Linford, J. Van der Maas, W. De Jeu, H. Zuilhof and E. Sudhölter, *Langmuir*, 1998, **14**, 1759–1768.
64 M. Yang, D. Huang, P. Hao, F. Zhang, X. Hou and X. Wang, *J. Appl. Phys.*, 1994, **75**, 651.
65 R. Tsu, H. Shen and M. Dutta, *Appl. Phys. Lett.*, 1992, **60**, 112.
66 J. Rouquerol, F. Rouquerol, P. Llewellyn, G. Maurin and K. S. Sing, *Adsorption by Powders and Porous Solids: Principles, Methodology and Applications*, Academic press, 2013.
67 U. Grüning and A. Yelon, *Thin Solid Films*, 1995, **255**, 135–138.
68 S. E. Wheeler, *J. Am. Chem. Soc.*, 2011, **133**, 10262–10274.
69 L. J. Riwar, N. Trapp, B. Kuhn and F. Diederich, *Angew. Chem.*, 2017, **56**, 11252–11257.
70 G. H. Al-Hazmi, V. Marrakkur, L. Naik and M. S. Refat, *Pol. J. Chem. Technol.*, 2024, **26**, 1–7.
71 P. Panini, E. Boel, L. Van Meervelt and G. Van den Mooter, *Cryst. Growth Des.*, 2022, **22**, 2703–2724.
72 A. Koll, V. Parasuk, W. Parasuk, A. Karpfen and P. Wolschann, *J. Mol. Struct.*, 2004, **700**, 81–90.
73 S. Scheiner, T. Kar and J. Pattanayak, *J. Am. Chem. Soc.*, 2002, **124**, 13257–13264.
74 E. M. Mahdi and J.-C. Tan, *J. Membr. Sci.*, 2016, **498**, 276–290.
75 R. Sogame, Y. J. Choi, T. Noda, K. Sawada and K. Takahashi, *Sensors*, 2024, **24**, 8055.
76 M. Gu, H. Chen and L. Li, *Sensor Actuator Phys.*, 2025, **387**, 116481.
77 N. Liu, X.-F. Wang, G. Zhang, H. Liang, T. Li, Y. Zhao, T. Zhang, Z. Tan and X.-Z. Song, *ACS Appl. Nano Mater.*, 2022, **5**, 14320–14327.